Available online at www.sciencedirect.com
ScienceDirect
Trans. Nonferrous Met. Soc. China 32(2022) 2634−2647
Transactions of Nonferrous Metals Society of China
www.tnmsc.cn

Effects of selective laser melting parameters on surface quality and densification behaviours of pure nickel

Tian-yang YUE[1], Sheng ZHANG[1,2], Chao-yue WANG[3], Wei XU[4], Yi-di XU[1], Yu-sheng SHI[5], Yong ZANG[1,2]

1. School of Mechanical Engineering, University of Science and Technology Beijing, Beijing 100083, China;
2. Shunde Graduate School, University of Science and Technology Beijing, Foshan 528300, China;
3. School of Materials Science and Engineering, University of Science and Technology Beijing, Beijing 100083, China;
4. Institute for Engineering Technology, University of Science and Technology Beijing, Beijing 100083, China;
5. State Key Laboratory of Materials Processing and Die & Mould Technology, School of Materials Science and Engineering, Huazhong University of Science and Technology, Wuhan 430074, China

Received 29 September 2021; accepted 4 March 2022

Abstract: The effects of laser power and scanning speed on the forming characteristic of scanning tracks, densification behaviours and surface roughness of pure nickel fabricated with selective laser melting (SLM) were studied. The results indicate that the scanning tracks showed continuous, regular and flat surface with increasing laser power and decreasing scanning speed in a specific range, which could avoid the defects (like holes and balling structures) forming in SLM processing. The optimal process window was identified as the scanning speed of 900 mm/s and the laser power of 255−275 W by comparing the surface qualities and densification behaviours. With the suitable processing parameters, the relative density could achieve 99.16%, the tensile strength was (359.49±2.74) MPa, and the roughnesses of the top and side surfaces were (12.88±2.23) and (14.98±0.69) μm, respectively.

Key words: selective laser melting; pure nickel; scanning track; densification; surface roughness

1 Introduction

Pure nickel has been widely applied in aerospace, chlor-alkali, navigation, and military industries, due to excellent corrosion and oxidation resistance, high thermal conductivity, and good magnetism and high-temperature stability [1,2]. With further development in the complexity of structural features of components, conventional methods cannot fully meet the high requirements for industrial components [3−6]. In recent years, additive manufacturing (AM) provides an economic approach to overcoming these limitations, since it enables the fabrication of three-dimensional complex-shaped components with high geometrical accuracy at reduced duration and cost [7]. As one of these promising additive manufacturing approaches, selective laser melting (SLM) technology uses high-intensity lasers as an energy source to melt and fuse selective regions layer by layer in a metal powder bed, which facilitates manufacturing bulk structures with novel and complex designs [8]. The flexibility in producing parts has made the SLM technology successful for application in fabricating dozens of metal materials such as steel, nickel-based alloys, titanium-based alloys, aluminium-based alloys, and metal matrix composites [9−11].

Despite the advantages of the SLM technology, there are always challenges, including the need for improving relative density, lowering surface roughness, and avoiding distortion of SLM-ed

Corresponding author: Sheng ZHANG, Tel: +86-15201599409, E-mail: zhangsheng@ustb.edu.cn
DOI: 10.1016/S1003-6326(22)65972-7

parts [12,13]. These forming qualities are highly dependent on laser energy input, which depends on the process parameters including laser power, scanning speed, and so on [14,15]. Obviously, optimizing the processing parameters is a direct and effective method to improve the density and surface quality of pure nickel parts fabricated by SLM. YAP et al [16] proposed a brief analytical SLM model by investigating the energy requirement in the pure nickel and titanium experiment. In their following work, near dense pure nickel blocks with a relative density of 98.9% were obtained by optimizing process parameters, and the mechanical properties were better than those of the traditionally processed pure nickel [17]. ZHAO et al [18] studied the electrochemical performance of the pure nickel blocks prepared by SLM under different laser energy densities, aiming to develop a new-type porous nickel electrode fabricated by SLM. ZHANG et al [19] used a novel method to prepare pure nickel powder with high laser absorption, which has been proven to be beneficial to fabricating more dense pure nickel blocks than using the commercial pure nickel powder. These studies evaluated the feasibility and practicality of the pure nickel parts processed by SLM, proving the application potential of the SLM-ed pure nickel parts. Nevertheless, previous studies have not delved into the variation tendency of the densification behaviours and surface quality of pure nickel during the SLM process. The densification behaviours and surface quality were highly affected by defects, including the different kinds of pores, the humps or edge distortion, and the unmelted powders. Discovering the variation trend of the defects with different process parameters was crucial to obtaining a more suitable process window for SLM-ed pure nickel parts. Hence, a further and more detailed process optimization to discover the variation tendency of the forming quality, including the densification and surface morphologies, of the SLM-ed pure nickel parts is still needed.

In addition, since SLM consisted of a track-by-track and a layer-by-layer process, the performance of the built block was largely dependent on the forming quality of the scanning tracks, which were mainly determined by the laser power and scanning speed [20,21]. The defects that appear on the scanning tracks could directly map to the blocks [22]. Therefore, discovering the forming regularities of scanning tracks and establishing the relationship between the scanning tracks and the forming quality of blocks are effective methods for optimizing the process window of the SLM-ed pure nickel part.

In this study, the scanning tracks and blocks of pure nickel were fabricated by SLM with different laser powers and scanning speeds. The variation of the formation and geometric characteristics of scanning tracks were investigated to discover the defects formation mechanism during SLM processing. The blocks were produced for the characterization of surface quality and densification to obtain an optimized process window. Hopefully, these results will provide a basic guide for the fabrication of high-quality SLM-ed pure nickel parts.

2 Experimental

2.1 Materials and SLM process

In this work, gas-atomized pure nickel powders were used as raw materials to produce SLM specimens (as shown in Fig. 1). The powders present an almost spherical shape (Fig. 1(a)), with the particle size D_{50}=49.80 μm (Fig. 1(b)). Table 1 lists the chemical composition of the pure nickel powder.

The specimens were fabricated using SLM equipment (EOSINT M280, Germany) with a Yb-fibre laser source under 400 W power and 100 μm laser spot. The SLM process was controlled by PSW 3.6 software and operated in an inert protection system. Before fabrication, a steel substrate was fixed on the building platform and levelled. Here, the substrate of 316L steel materials was chosen due to its high content of Fe element with a good wettability for pure nickel. Then, pure nickel powders were laid layer by layer; the laser selectively scanned the powders according to computer-aided design (CAD) data after every layer was completely laid. A range of process parameters was used to build cube specimens and scanning tracks. Finally, the specimens with a dimension of 6 mm × 6 mm × 8 mm were fabricated to characterize the morphology and densification. Based on the commonly applied process parameters of SLM-ed Ni-based materials in previous studies [23], the process parameters were designed

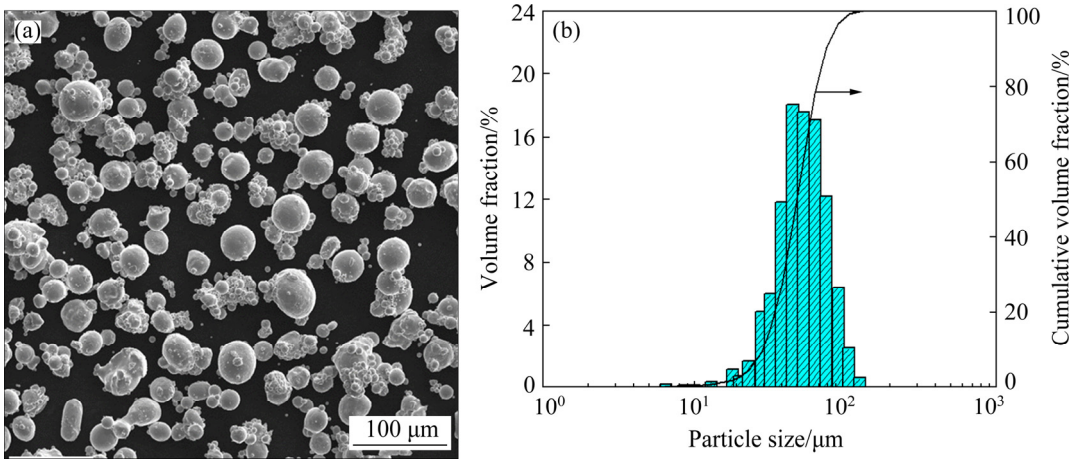

Fig. 1 Characteristics of pure nickel powders: (a) Morphology; (b) Particle size distribution

Table 1 Chemical composition of pure nickel powders (wt.%)

Ni	Co	C	Si	P
Bal.	0.012	0.0014	0.0012	0.001
S	Fe	Cu	Zn	
0.001	0.002	0.003	0.001	

in this experiment via the orthogonal experiment. As shown in Fig. 2, the scanning speed was from 700 to 1300 mm/s with the interval of 200 mm/s, the laser power was from 235 to 295 W with the interval of 10 W, and the layer thickness and hatching spacing were fixed at 40 μm and 90 μm, respectively. According to Eq. (1), the process window (D) was defined:

$$D=\frac{P}{\nu ht} \tag{1}$$

where P is the laser power, ν is the scanning speed, h is the hatching space, and t is the layer thickness [22]. This process window corresponds to a laser energy density from 50.21 to 117.06 J/mm^3 with an average interval less than 2.5 J/mm^3, which helps to avoid missing the optimal processing parameter. To reduce the residual stress, scanning strategy of a zigzag pattern with a 67° rotation between every two layers was adopted. The substrate is preheated to 80 °C during processing.

2.2 Characterizations

The surface morphologies of the samples were imaged by a scanning electron microscope (SEM, Phenom Prox, Netherlands) and a laser scanning confocal microscope (Olympus 4000, Japan). The surface roughness (R_a) of the specimens was measured by a rough meter (Surftest SJ−210, China). The measure direction on the top surface was perpendicular to the laser scanning direction to obtain the maximum R_a, and the measure direction on the side surface was parallel to the building direction. The relative density of the specimens was calculated based on the Archimedes principle employing Eq. (2):

$$\frac{\rho_{\mathrm{SLM}}}{\rho_{\mathrm{standard}}}=\frac{\rho_{\mathrm{water}}\cdot m_{\mathrm{SLM(air)}}}{\rho_{\mathrm{standard}}\left(m_{\mathrm{SLM(air)}}-m_{\mathrm{SLM(water)}}\right)} \tag{2}$$

where ρ_{SLM} is the density of SLM-ed pure nickel samples, ρ_{standard} is the theoretical density of pure nickel (8.9 g/mm^3), $m_{\mathrm{SLM(air)}}$ is the mass of the SLM sample in air, $m_{\mathrm{SLM(water)}}$ is the mass of the SLM sample in deionized water, and ρ_{water} is the density of the deionized water. The horizontal and vertical cross-sections of the samples were mirror-finished and etched for about 10 s in corrosive reagent (2 mL H_2O + 10 mL HNO_3 + 10 mL $C_2H_4O_2$) at room temperature for microstructural observation. The tensile tests were conducted at room temperature on a testing machine (CMT5105, China) at a cross-head velocity of 1 mm/min.

3 Results and discussion

3.1 Geometric characteristics of scanning tracks

Figure 3 shows the surface morphologies of scanning tracks at different laser powers and scanning speeds. In Fig. 3, the processing window was divided into three regions from the geometric characteristics of morphologies and continuity of

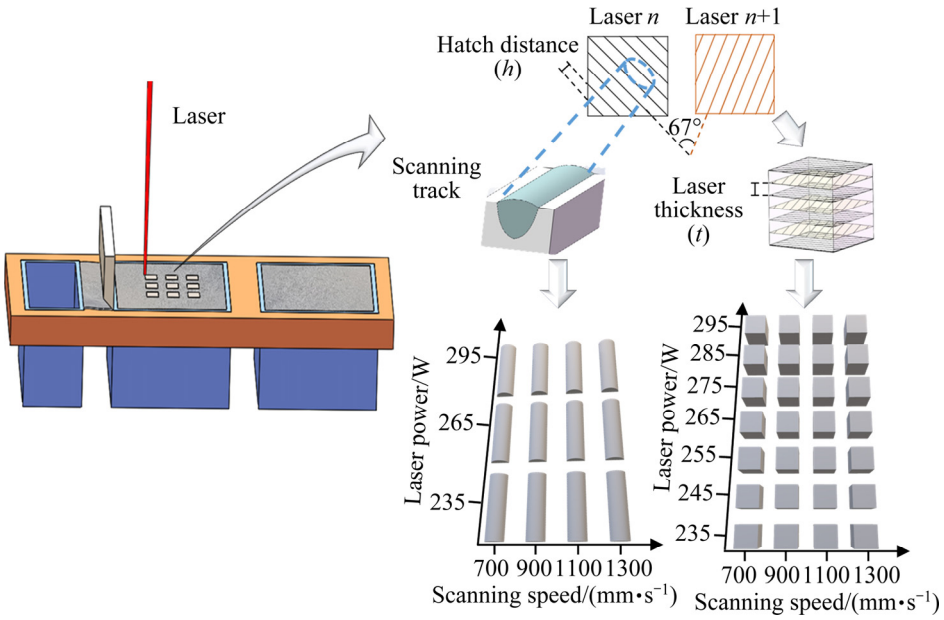

Fig. 2 Illustration of SLM processing pure nickel powders

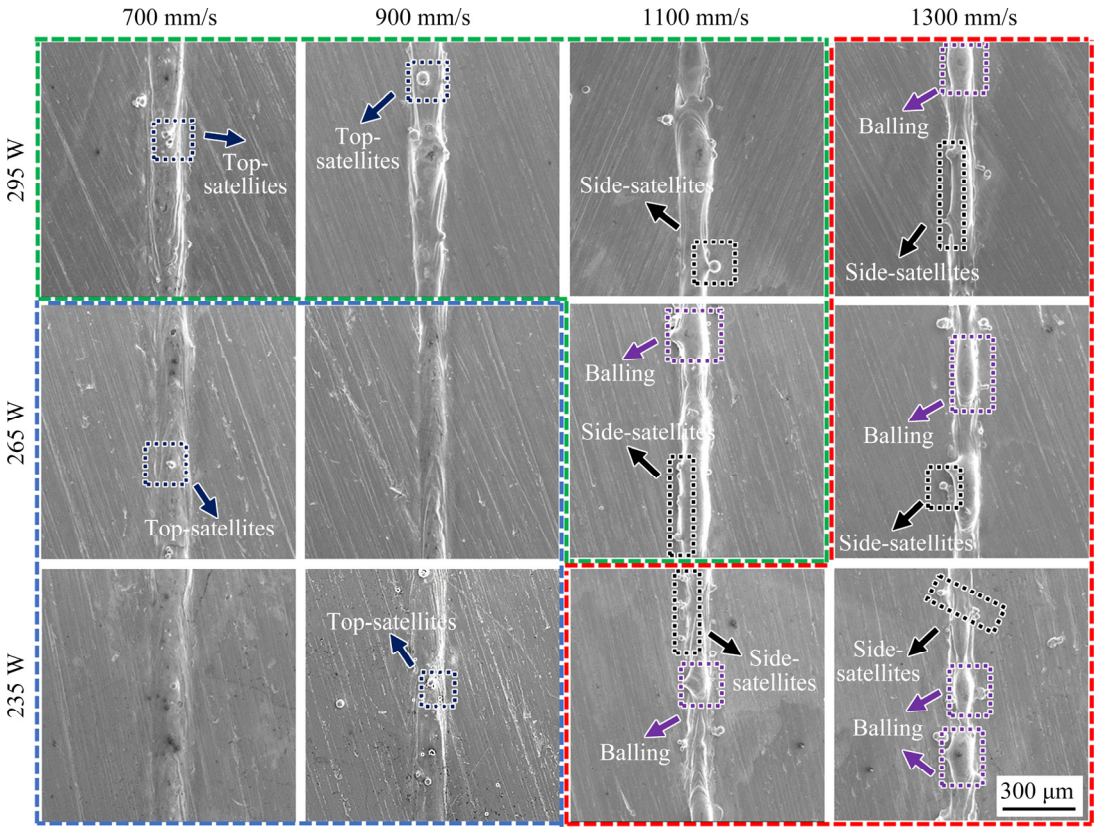

Fig. 3 Surface topographies of scanning tracks with different process parameters

scanning tracks. These regions constituted the discontinuous region (the red-dashed rectangle in Fig. 3), the irregular region (the green-dashed rectangle in Fig. 3), and the regular region (the blue-dashed rectangle in Fig. 3). This clearly illustrated that the surface morphologies were significantly dependent on the laser power and scanning speed. At the high scanning speed and low laser power, narrow scanning tracks with undulate and typical balling phenomena were formed in the discontinuous region. The serious balling effect broke the continuity of the scanning tracks and

caused the irregular shape of the scanning tracks, indicated by purple-dashed rectangles. Besides, some powder particles distributed around or stuck to the side of the scanning tracks (indicated by black-dashed rectangles), which were defined as side-satellites [24,25]. The side-satellites showed poor solidification characters and were primarily caused by the partially melted particles. This phenomenon would promote unqualified bonding between adjacent tracks during the following SLM processing [24]. Increasing the laser power or decreasing the scanning speed would retrain the balling and side-satellites, as shown in the irregular and regular regions. Particularly in the regular region, the scanning tracks presented a regular shape with a smooth edge. However, in the irregular region, the scanning tracks with irregular shapes were also formed at the high laser power of 295 W and the low scanning speeds of 700 and 900 mm/s, meaning that laser energy input was excessively high. In addition, there were some powders on the scanning tracks in the regular and irregular regions, indicated by the mazarine-dashed rectangles. These powders, defined as top-satellites, were mainly induced by the spattering of molten pools, which could not be avoided completely [25].

The serious balling phenomena not only disrupted the continuity of the tracks, but also greatly increased the height of the scanning tracks. Three-dimensional surface topographies of the scanning tracks are illustrated in Fig. 4, where the scanning tracks are mainly represented by the green zone. More irregular and uneven surface morphologies were formed at 1300 mm/s, as shown in Figs. 4(d−f), and the height of the laser track surfaces at 1300 mm/s ranged from 70 to 110 μm, larger than 50−80 μm at 700 mm/s, as shown in Figs. 4(a−c). The results also demonstrated that the scanning tracks were narrow under high scanning speed conditions. Figure 5 exhibits the width of the scanning tracks. It could be seen that the width sharply decreased with the increase of scanning speed. At 700 mm/s, the widths of the scanning tracks exceeded 150 μm, while these widths stayed below 110 μm at 1300 mm/s.

Based on the above experimental phenomena, it could be found that the forming characteristics of the scanning tracks were inferior under high scanning speed and low laser power. This could be caused by the poor flowability of the molten pool which was induced by the insufficient laser energy input. At the scanning speed of 1100−1300 mm/s and the laser power of 235−265 W, the laser energy density was below 70 J/mm^3. The low laser energy density would decrease the operative temperature significantly [26,27]. In this situation, a small number of powders was completely melted into the liquid phase, thus forming a narrow molten pool. In addition, the operative temperature of the molten pool determined the dynamic viscosity (η_v) of the liquid phase in the molten pool [28]:

$$\eta_v = \frac{16}{15}\sqrt{\frac{m}{kT}}\sigma \tag{3}$$

where m is the atomic mass, k is the Boltzmann constant, T is the molten pool temperature, and σ is the surface tension which is inversely proportional to T. According to this equation, high dynamic viscosity of the pure nickel liquid was obtained when the insufficient laser energy density induced a low operative temperature. As a result, the metal liquid would not adequately spread and wet the

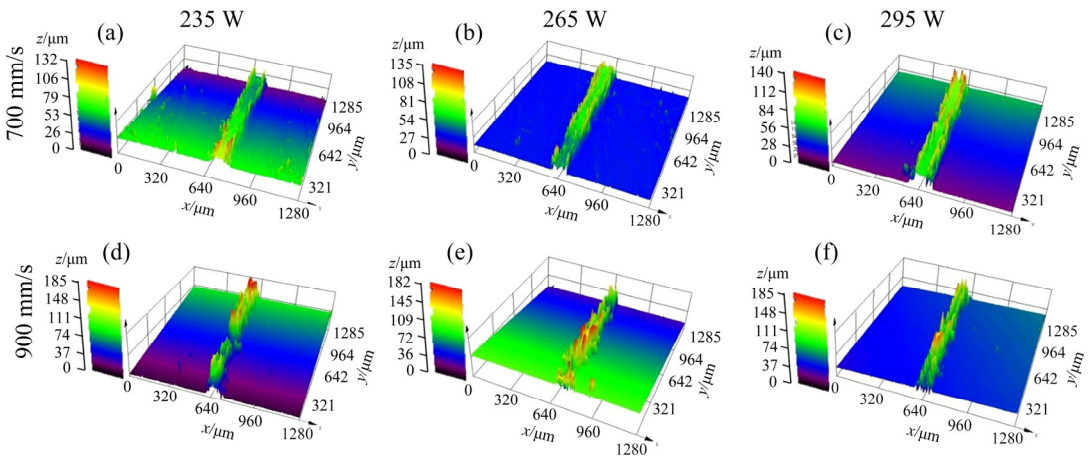

Fig. 4 Three-dimensional morphologies of scanning tracks with different laser powers and different scanning speeds

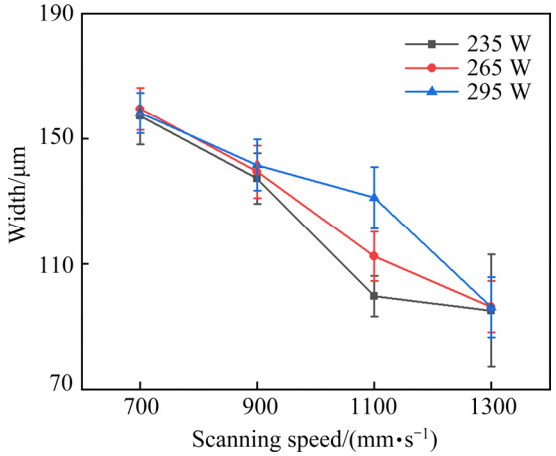

Fig. 5 Width of scanning tracks with different processing parameters

unmelted powders around the molten pools. This would also limit the contact area between the molten pool and the substrate. Under high surface tension σ, the direction of liquid flow was prone to be inward, thus resulting in the liquid to spheroidize towards the contact area and the formation of balling [29].

In addition, as shown in Fig. 3, distorted and uneven scanning tracks were formed at 295 W, 1100 mm/s (74.49 J/mm^3) while smooth, regular scanning tracks were formed at 235 W, 900 mm/s (72.53 J/mm^3). The scanning tracks formed at high scanning speed would deteriorate compared to those at low scanning speed under the similar laser energy density conditions. This could be explained as the result of the liquid phase within the molten pool having not enough time to flow and spread at high scanning speed [21].

3.2 Top surface morphologies of SLM blocks

Figure 6(a) shows the optical images of the top surface of pure nickel blocks and Fig. 6(b) shows the corresponding surface roughness. According to Fig. 6(a), specimens were successfully fabricated without defects such as burning loss or surface corrugation, which would destroy the forming quality and hinder the following recoating of powder. The result proved that the selected process window was suitable for acquiring a structurally sound specimen. This also clearly illustrated that the sintering formability of specimens was closely connected to the process parameters. The smooth and bright surface topographies were achieved when the scanning speeds were 700 and 900 mm/s (blue and green regions). As shown in the blue region, the surface roughness (R_a) of all specimens was below 14 μm and the average value was 10.99 μm. Particularly, the lowest value of 7.87 μm was obtained at 265 W, 700 mm/s. Further increasing the scanning speed contributed to the worsening of the surface quality of the specimens, which presented coarse and uneven surface morphologies as shown in the yellow and red regions. The R_a of all specimens in the red region was over 20 μm and the average value reached 22.76 μm. Besides, the low laser power also induced a poor surface quality. Specimens fabricated at 235−255 W were found to exhibit higher surface roughness than those with higher laser power. In addition, it was also found the edge distortion on the top surface at the scanning speed of 700 mm/s, meaning the low scanning speed could also induce other defects.

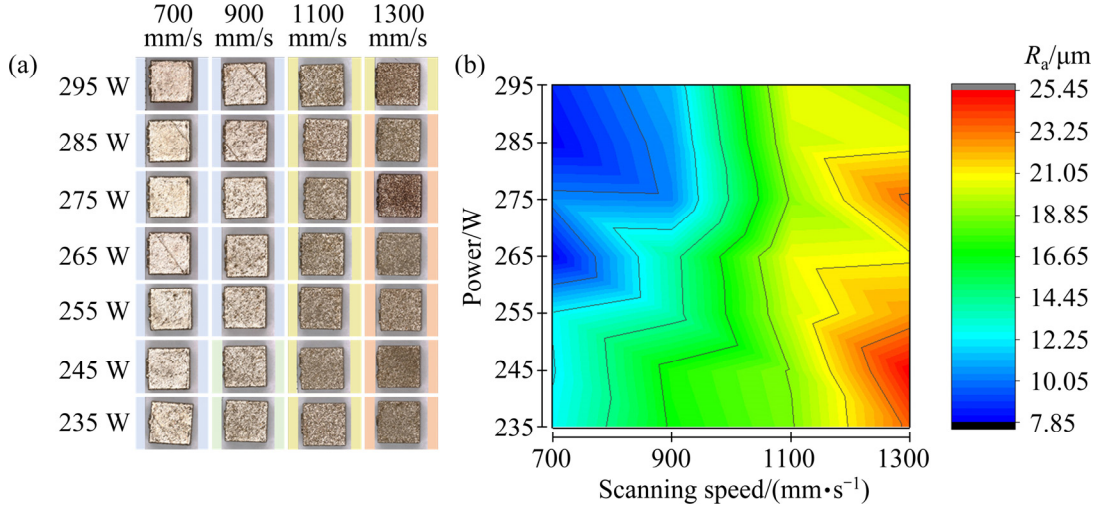

Fig. 6 Optical images of pure nickel blocks fabricated by SLM (a) and corresponding surface roughness (b)

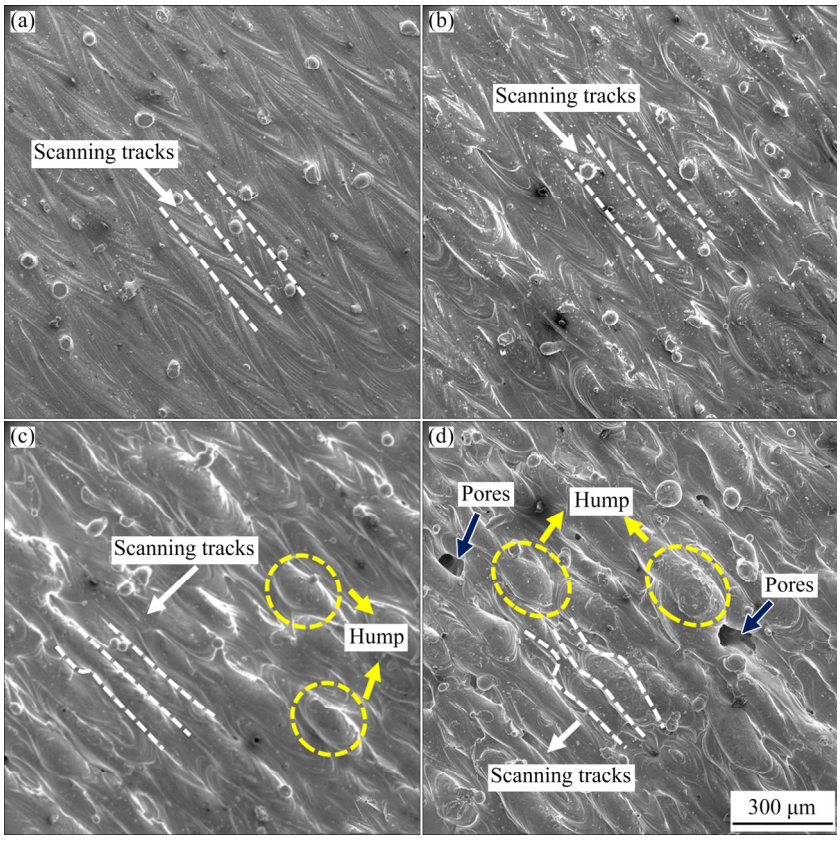

Fig. 7 SEM images showing typical top surface morphologies of specimens prepared at different scanning speeds and laser power of 265 W: (a) 700 mm/s; (b) 900 mm/s; (c) 1100 mm/s; (d) 1300 mm/s

Figure 7 illustrates the SEM images of surface topographies of blocks formed at 265 W with various scanning speeds. The white lines indicate adjacent tracks on the top surface. It could be concluded that the surface quality was primarily dependent on the solidification characters of scanning tracks. At low scanning speeds (700 and 900 mm/s), the surface consisted of smooth and regular scanning tracks without balling defects, corresponding to good surface morphologies of scanning tracks formed at a high laser energy density. Besides, the overlap between adjacent scanning tracks was sufficient in this condition. According to Fig. 8 and Eq. (4) [30], there was

$$z=\frac{a}{L}=\frac{L-h}{L} \tag{4}$$

where z is the overlap ratio of the scanning tracks, a is the length of the overlap region between adjacent scanning tracks, and L is the width of the laser track. The overlap ratio is proportional to the width of the scanning track. When high laser energy input was absorbed by the molten pool, the good flowability and spreadability easily solidified the molten pool

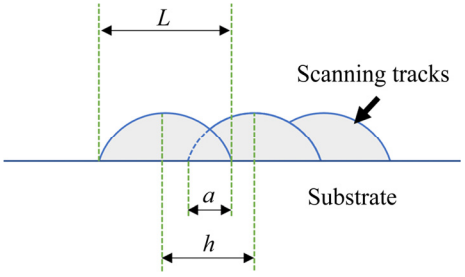

Fig. 8 Schematic diagram of overlap ratio of scanning tracks

into regular scanning tracks with a large width, as proven in Fig. 3 and 5, thereby achieving a high overlap ratio. The high overlap ratio would increase the quantity of re-melting for materials, thus lengthening the solidification time [21]. The liquid phase had enough time to spread, leading to optimum bonding between adjacent tracks, and hence smooth surface morphologies were formed. At large scanning speeds (1100 and 1300 mm/s), laser energy input was insufficient and the spreading properties of the liquid phase within the molten pool deteriorated. The size of the scanning tracks was small, making the overlapping

conditions of the adjacent scanning tracks insufficient. Moreover, the laser track was irregular and even separated by balling initiation. As a result, the surface formation was so poor that it induced holes, irregular bonding of adjacent scanning tracks, and distinct humps on the surface.

From the results of surface roughness, the top surface of the block formed at 295 W, 1100 mm/s was coarser than that formed at 295 W, 900 mm/s. Figures 9(a, b) show the SEM images of the surface topographies of the two blocks, respectively. The obviously distorted bonding of scanning tracks, and serious balling formed on the surface of the specimens prepared at 295 W, 1100 mm/s could be observed. This experiment corresponded to the result of the scanning tracks, which proved that a high scanning speed would lead to a worse surface quality than that formed at a low scanning speed when the laser energy density is approximate.

Besides, a slightly warped distortion existed on the edge of the specimens in a process window of 235−295 W, 700 mm/s by direct visual observation. Figure 10 shows the optical image of the samples formed at 700 and 900 mm/s. Figure 11 shows the corresponding three-dimensional morphologies of the edge region and the accurate height of the edge

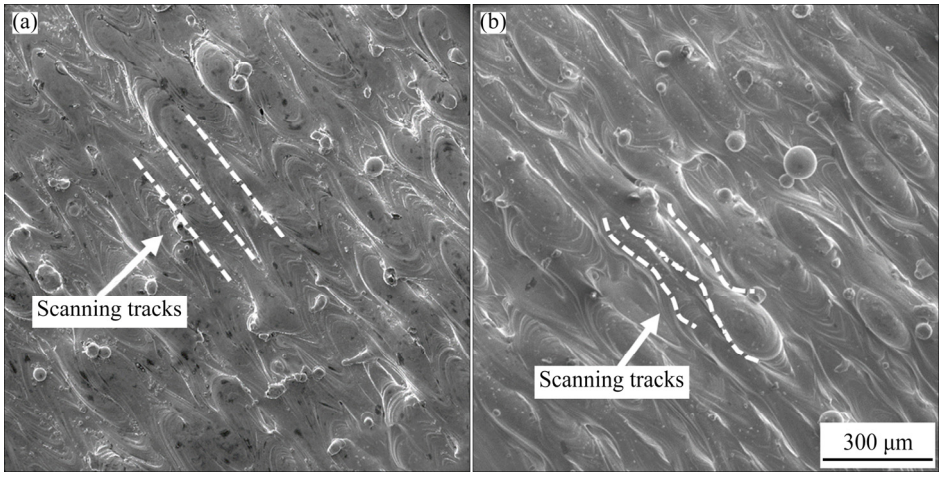

Fig. 9 SEM images showing typical surface morphology of specimens at similar laser energy density: (a) 72.53 J/mm^3, 235 W, 900 mm/s; (b) 74.49 J/mm^3, 295 W, 1100 mm/s

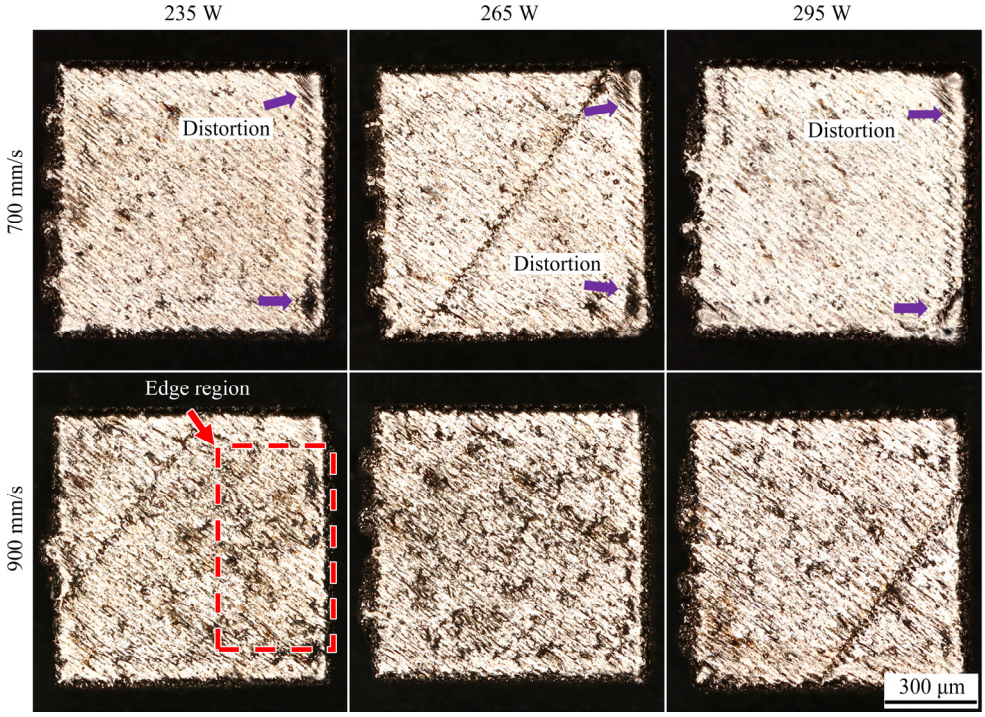

Fig. 10 Optical images of samples at different laser powers and different scanning speeds

region obtained from the three-dimensional morphologies. Comparing the three-dimensional morphologies and the height exhibited a more obvious distorted edge at the scanning speed of 700 mm/s, which not only made the geometric dimension of the specimens inaccurate but also affected the following motion of the coater blade and even prematurely terminated the SLM process if it became serious [31−33]. This mainly resulted from the tensile stress near the top surface. The larger the laser energy input was, the higher the temperature gradients were in the SLM process, thus producing higher thermal stress in the blocks [32]. When the laser energy was enlarged, the warp distortion would be induced by the high thermal stress [33].

3.3 Side surface morphologies of SLM blocks

The side surface quality is also a pivotal factor for the SLM-ed specimens, because it not only influences the size accuracy but also determines the complexity of the post surface finishing for the specimens. Figure 12 illustrates the roughness variation on the side surface of blocks. The side surface roughness presented a similar variable tendency to the result of the top surface roughness. The lower R_a was also obtained at high laser energy density with the scanning speeds of 700 and 900 mm/s, and the R_a was in the range from 13.49 to 15.68 μm; all the values were close. When decreasing the laser energy density, the R_a was in the range of 15.90−19.30 μm. Figure 13 shows the side-surface topographies of the blocks prepared at 265 W. Compared to the top surface topographies, side surface exhibited a different influencing mechanism on the surface roughness. There was a large quantity of powders randomly sticking to the side surface of all specimens. This was the primary reason for the deterioration of surface roughness, and a similar phenomenon was found in other previous studies [24]. At 700 and 900 mm/s, it could easily be observed that the molten pools overlap regularly (marked by yellow-dashed curves), which meant that the surface would be flat if no powders stick to it. At 1100 and 1300 mm/s, the molten pools could not be observed easily and some unsolidified humps induced by an insufficient laser energy density appeared on the surface (marked by yellow-dashed circles), making the surface uneven; the R_a would be enlarged.

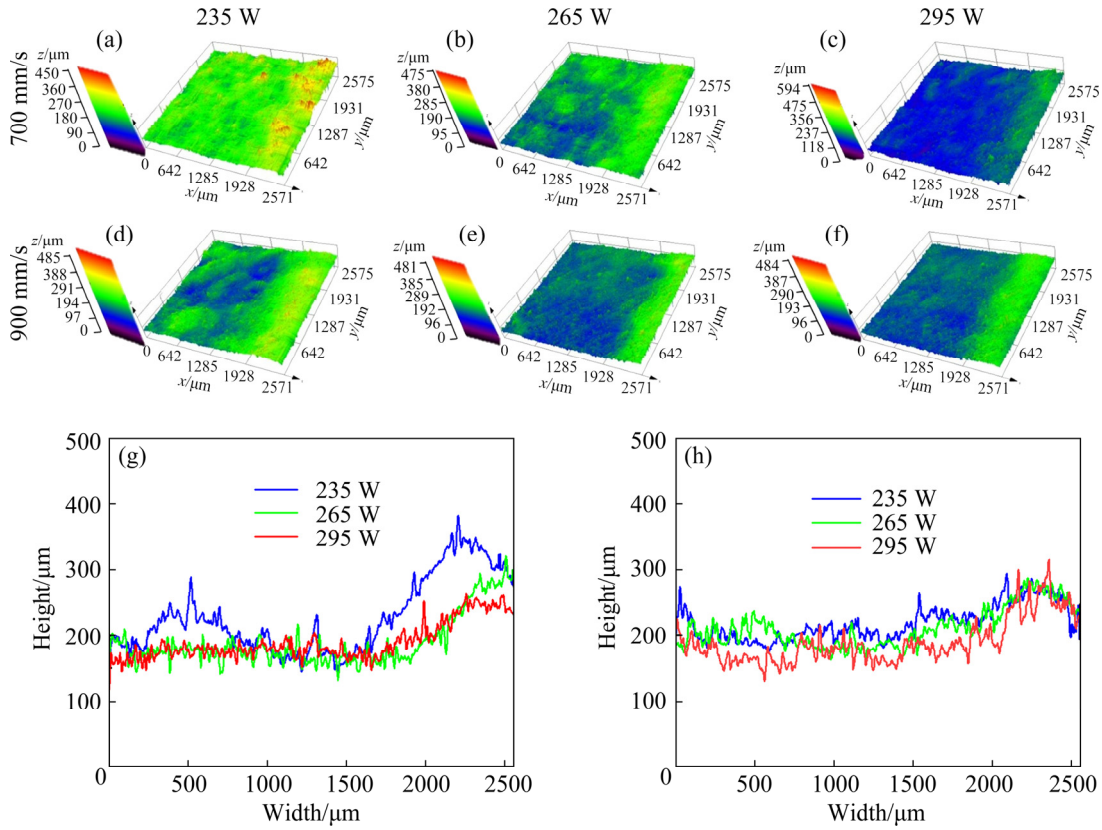

Fig. 11 Morphologies and height distribution of edge region on top surface: (a−f) Corresponding three-dimensional morphologies; (g, h) Height distribution at 700 mm/s and 900 mm/s, respectively

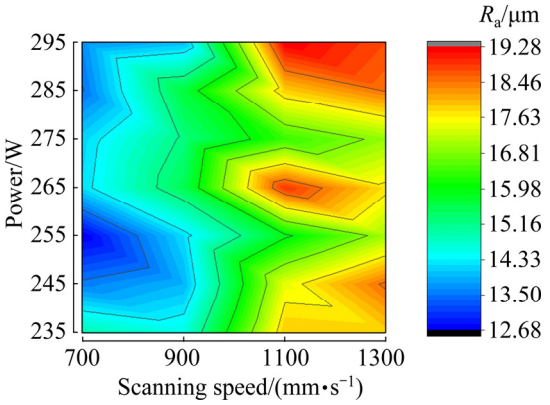

Fig. 12 Side surface roughness of blocks

3.4 Densification behaviour

Figure 14 illustrates densification behaviours of the specimens. As shown in Fig. 14(a), the densities of the specimens evaluated by the Archimedes method were in the range of 8.49−8.83 g/cm^3, which corresponded to the relative densities of 95.38%−99.22% shown in Fig. 14(b). The results revealed that the densifications of the specimens increased initially and then reduced with increasing laser energy density. It could be concluded that the high dense blocks formed in the suitable range of 71.97−101.19 J/mm^3, particularly 75.62−84.88 J/mm^3 (corresponding to 245−285 W

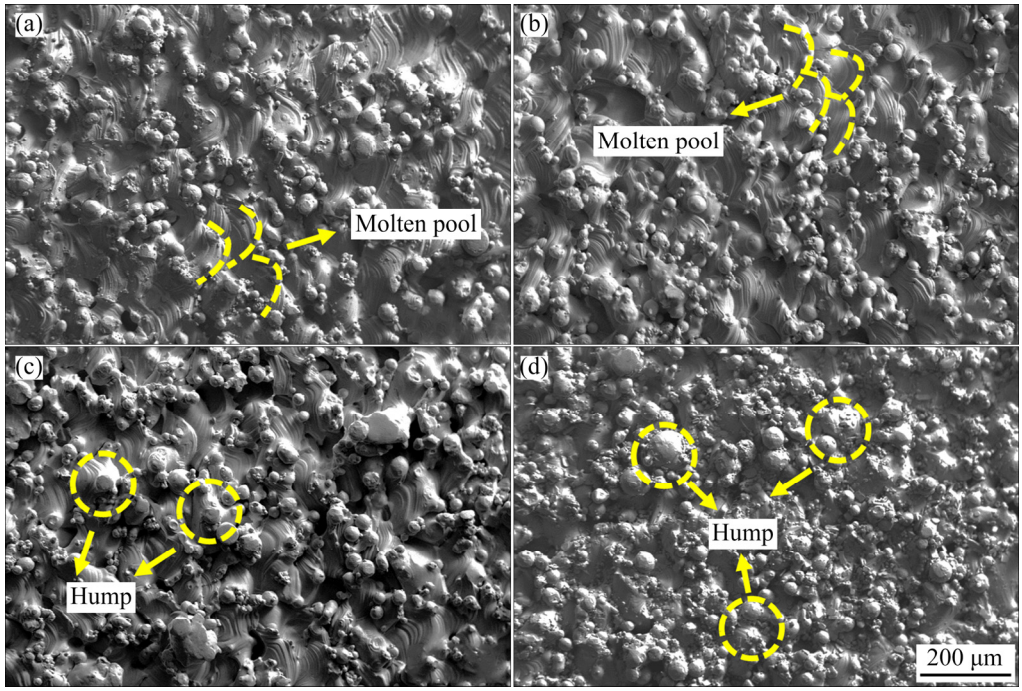

Fig. 13 SEM images of side surface morphologies of specimens prepared at laser power of 265 W and different scanning speeds: (a) 700 mm/s; (b) 900 mm/s; (c) 1100 mm/s; (d) 1300 mm/s

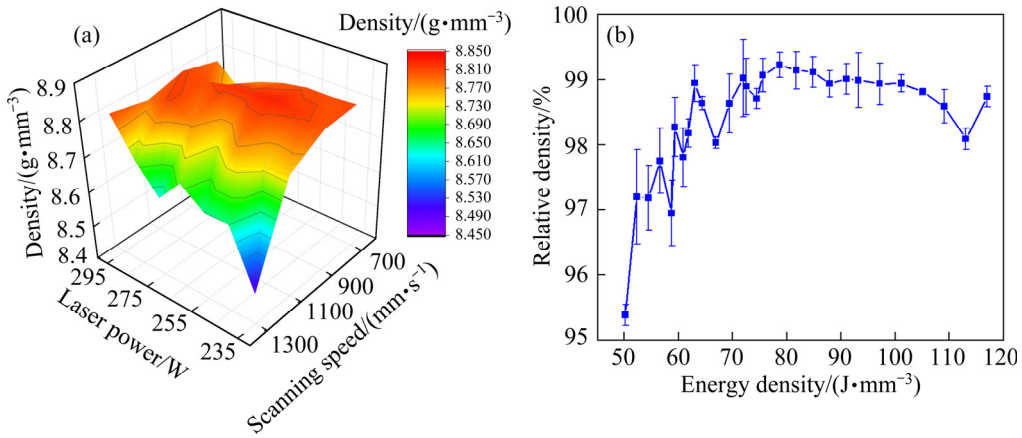

Fig. 14 Densification behaviours of specimens at different laser powers and scanning speeds (a) and corresponding relative density at different laser energy densities (b)

and 900 mm/s), had an excellent densification behaviour where all the densities of the blocks were above 8.82 g/cm^3 (relative density of 99.10%).

Figure 15 shows the polished surfaces of the specimens prepared with different process parameters. This distinctly exhibited that plenty of pores mainly concentrated at the surface of the specimens prepared with high scanning speed and low power. Besides, the morphologies, including the shape and size of these pores, varied as the process parameters were changed. At 235 W, 1300 mm/s, the largest numbers of pores covered the surface of the specimens. These pores were long and in polygynous shape, and some of them had a size larger than 100 μm (indicated by red-dashed rectangles). Therefore, the poor densification performance of the as-built blocks was induced. Increasing the laser power or reducing the scanning speed would weaken the forming of the pores; not only the number of pores decreased but also the size of the pores reduced. At the same time, the proportion of the irregular pores gradually decreased and the pores in the quasi-circular shape (indicated by black-dashed circles) started to form on the surface. At 900 mm/s, 235−295 W, there were almost no obvious pores on the surface, and high dense blocks were achieved. However, the number of circular pores presented an incremental tendency at 700 mm/s, 265 W, and 295 W, which meant that the densification behaviours were also poor in excessive laser energy input conditions.

The irregular pores are commonly referred to the lack of fusion [28], which was ascribed to the insufficient laser energy input. From the results of the scanning tracks in Fig. 3, when the laser energy input was too low to melt sufficient powders, narrow and unstable scanning tracks with the balling phenomena were formed. Accordingly, the bonding of adjacent tracks became poor and irregular, and the deposited layer was considerably uneven. Therefore, the following powder deposition would have poor uniformity. As the laser scanned a rugged powder layer, the molten pools were unstable with various defects, including balling and discontinuity, thereby inducing the formation of irregular pores. In addition, the low laser energy density also led to the small penetration depth of molten pools. As shown in Fig. 16, the outlines of the molten pools are marked by black-dashed curves. It could be seen that the molten pools formed at 69.44 J/mm^3 had a smaller penetration depth than those formed at 81.79 and 117.06 J/mm^3. This was caused by the insufficient remelt on the pre-deposited layers. Once the pores were formed, it would be difficult to eliminate these pores in the following deposition process because the liquid phase was not enough to fill it. The quasi-circular pores mainly formed at high laser energy density were defined as gas pores [34,35]. Two main reasons accounted for the formation of gas pores. One was the trapping of protective gas (here Ar); high laser energy input led to an excellent flowability of the molten pool which rolled the Ar easily in the liquid materials. The second reason

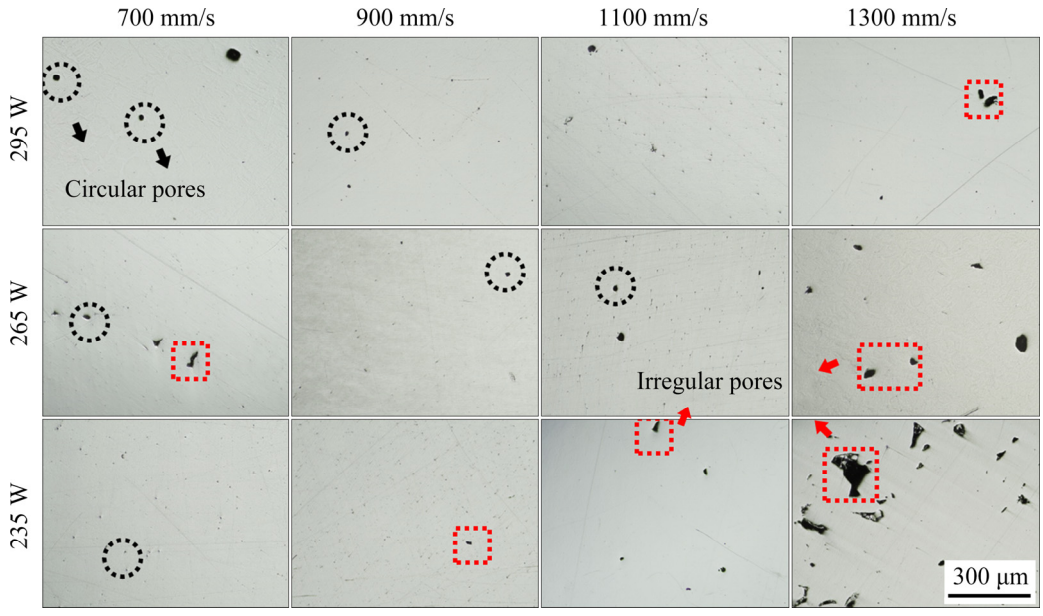

Fig. 15 Optical images of polished surface with different process parameters

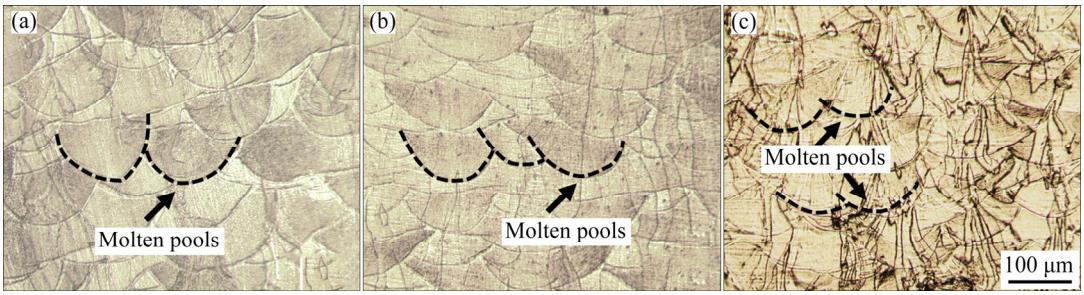

Fig. 16 Molten pools on side surface of blocks at different laser energy densities: (a) 117.06 J/mm^3; (b) 81.79 J/mm^3; (c) 69.44 J/mm^3

was the metal vapor produced during the melting process; the temperature of the molten pool went up with increasing energy input, inducing the evaporation of the metal powder [34].

3.5 Tensile properties

The tensile test has been conducted at the dense specimens fabricated at the laser power of 265 W and the scanning speed of 900 mm/s. The cylinders were horizontally fabricated and machined into standard tensile samples with the size of d5 mm × 60 mm according to Chinese National Standard GB/T 228.1—2010. The yield strength ($\sigma_{0.2}$), tensile strength (σ_m) and elongation (A_5) were (359.49±2.74) MPa, (286.16±4.07) MPa and (53.67±1.53)%, respectively. Compared with the tensile performance of N4 materials in the Chinese National Standard GB/T 4435 — 2010 (σ_m≥380 MPa, A_5≥34%), the ductility of SLM-ed pure nickel was satisfactory and the tensile strength was a little lower. This is because the pure nickel powder used in this experiment belongs to the N2 pure nickel which has a high purity of nickel element with little reinforcement element. Figure 17 shows the fracture samples. The apparent necking characteristic showed the high ductility achieved,

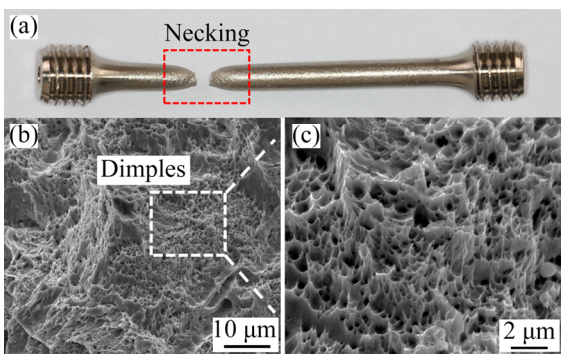

Fig. 17 Optical image of fracture samples (a), and SEM images of fracture surface (b, c)

and a large quality of dimples on the fracture surface indicated a typical ductile fracture model. In addition, no obvious defects were observed on the fracture surface, indicating good densification behaviours.

3.6 Demonstrative parts of as-fabricated pure nickel

Based on the optimized processing parameters, in particular, at the scanning speed of 900 mm/s, a pure nickel blade was successfully fabricated by SLM (as exhibited in Fig. 18). The as-fabricated pure nickel turbine has a size of 48.63 mm × 48.63 mm × 19.98 mm and some external flow channels on its surface, proving that the SLM technique has the unique capability to process complex pure nickel products with good surface finishing and geometrical precision. The results provide the possibility of commercialized prospects for SLM-ed pure nickel parts in the near future.

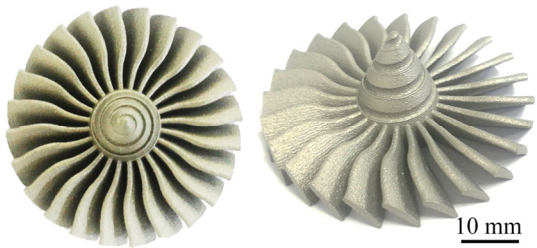

Fig. 18 Demonstrative part of SLM-ed pure nickel blade

4 Conclusions

(1) The scanning tracks presented a good geometrical characteristic when the laser scanning speed was varied from 700 to 900 mm/s and laser power was varied from 235 to 265 W, and at this time, the balling structures, irregular shape, and side-satellites were eliminated.

(2) Due to the low overlap ratio between

scanning tracks, the lack of fusion pores mainly took place at the scanning speed of 1100−1300 mm/s and laser power of 235−265 W, whereas the gas pores were mainly formed at the scanning speed of 700 mm/s and laser power of 265−295 W, owing to the metal evaporation and the gas into molten pools.

(3) SLM was used to produce pure Ni blocks with high density (>99%) and high geometrical precision. The optimum processing window identified in this work was the scanning speed of 700 mm/s and laser power of 255−275 W by comparing the surface qualities and densification behaviours.

Acknowledgments

This work is financially supported by the Scientific and Technological Innovation Foundation of Foshan, China (No. BK20BE011) and the Fundamental Research Funds for the Central Universities, China (No. FRF-GF-20-10B).

References

[1] CHOUDHURY I A, ELBARADIE M A. Machinability of nickel-base super alloys: A general review [J]. Journal of Materials Processing Technology, 1998, 77: 278−284.

[2] MENG Guo-zhe, SHAO Ya-Wei, ZHANG Tao, ZHANG Yi, WANG Fu-hui. Synthesis and corrosion property of pure Ni with a high density of nanoscale twins [J]. Electrochimica Acta, 2008, 53: 5923−5926.

[3] DIVINSKI S V, REGLITZ G, ROESNER H, YURI E, GERHARD W. Ultra-fast diffusion channels in pure Ni severely deformed by equal-channel angular pressing [J]. Acta Materialia, 2011, 59: 1974−1985.

[4] LEE T R, CHANG C P, KAO P W. The tensile behavior and deformation microstructure of cryo-rolled and annealed pure nickel [J]. Materials Science and Engineering A, 2005, 408: 131−135.

[5] FUJI A, HORIUCHI Y, YAMAMOTO K. Friction welding of pure titanium and pure nickel [J]. Science and Technology of Welding and Joining, 2005, 10: 287−294.

[6] HUO Hong-wei, LI Ying, WANG Fu-hui. Corrosion of AZ91D magnesium alloy with a chemical conversion coating and electroless nickel layer [J]. Corrosion Science, 2004, 46: 1467−1477.

[7] ZHANG H M, GU D D, MA C L, GUO M, YANG J K, ZHANG H, CHEN H Y, LI C P, SVYNARENKO K, KOSIBA K. Understanding tensile and creep properties of WC reinforced nickel-based composites fabricated by selective laser melting [J]. Materials Science and Engineering A, 2020, 802: 140431.

[8] WANG P, ECKERT J, PRASHANTH K G, WU M W, SCUDINO S. A review of particulate-reinforced aluminum matrix composites fabricated by selective laser melting [J]. Transactions of Nonferrous Metals Society of China, 2020, 30(8): 2001−2034.

[9] JU Jiang, LI Jing-jing, JIANG Min, YANG Li-xiang, WANG Kai-ming, YANG Chao, KANG Mao-dong, WANG Jun. Microstructure and electrochemical corrosion behavior of selective laser melted Ti6Al4V alloy in simulated artificial saliva [J]. Transactions of Nonferrous Metals Society of China, 2021, 31(1): 167−177.

[10] SING S L, YEONG W Y, WIRIA F E, TAY B Y, ZHAO Z Q, ZHAO L, TIAN Z L, YANG S F. Direct selective laser sintering and melting of ceramics: A review [J]. Rapid Prototyping Journal, 2017, 23(3): 611−623.

[11] HU Yong, YANG Xiao-kang, KANG Wen-jian, DING Yu-tian, XU Jia-yu, ZHANG Hui-ying. Effect of Zr content on crack formation and mechanical properties of IN738LC processed by selective laser melting [J]. Transactions of Nonferrous Metals Society of China, 2021, 31(5): 1350−1362.

[12] YANG T, LIU T T, LIAO W H, MACDONALD E, WEI H L, CHEN X Y, JIANG L Y. The influence of process parameters on vertical surface roughness of the AlSi10Mg parts fabricated by selective laser melting [J]. Journal of Materials Processing Technology 2019, 266: 26−36.

[13] AGRAWAL A K, BELLEFON G M, DAN T. High-throughput experimentation for microstructural design in additively manufactured 316L stainless steel [J]. Materials Science and Engineering A, 2020, 793: 139841.

[14] GHAYOOR M, LEE K, CHANG C H, PAUL B K, PASEBANI S. Selective laser melting of 304L stainless steel: Role of volumetric energy density on the microstructure, texture and mechanical properties [J]. Additive Manufacturing, 2020, 32: 101011.

[15] MOUSSAOUI K, RUBIO W, MOUSSEIGNE M, SULTAN T, REZAI F. Effects of selective laser melting additive manufacturing parameters of Inconel 718 on porosity, microstructure and mechanical properties [J]. Materials Science and Engineering A, 2018, 735: 182−190.

[16] YAP C Y, CHUA K C, DONG Z L. An effective analytical model of selective laser melting [J]. Virtual and Physical Prototyping, 2016, 11: 21−26.

[17] YAP C Y, TAN H K, DU Z L, CHUA C K, DONG Z L. Selective laser melting of nickel powder [J]. Rapid Prototyping Journal, 2107, 23: 750−757.

[18] ZHAO Yun, ZHAO Guo-rui, MA Wen-you, ZHENG Li, LIU Min. Study on process, microstructure and properties of Nickel fabricated by selective laser melting [J]. Laser and Optoelectronics Progress, 2020, 676: 186−197. (in Chinese)

[19] ZHANG Ya-juan, WANG Hai-bin, SONG Xiao-yan, NIE Zuo-ren. Preparation and performance of spherical Ni powder for SLM processing [J]. Acta Metallurgica Sinica, 2018, 54: 1833−1842. (in Chinese)

[20] YADROITSEV I, GUSAROV A V, YADROITSAVA I, SMUROV I. Single track formation in selective laser melting of metal powders [J]. Journal of Materials Processing Technology, 2010, 210(12): 1624−1631.

[21] BI Jiang, LEI Zheng-long, CHEN Yan-bin, CHEN Xi, QIN Xi-kun, TIAN Ze. Effect of process parameters on formability and surface quality of selective laser melted Al−Zn−Sc−Zr alloy from single track to block specimen [J]. Optics and Laser Technology, 2019, 118: 132−139.

[22] EL-SAYED M, GHAZY M, YOUSSEF Y, ESSA K. Optimization of SLM process parameters for Ti6Al4V medical implants [J]. Rapid Prototyping Journal, 2019, 25: 433−447.
[23] ZHANG Luo, LI Ye-tao, ZHANG Sheng, ZHANG Qing-dong. Selective laser melting of IN738 superalloy with a low Mn+Si content: Effect of energy input on characteristics of molten pool, metallurgical defects, microstructures and mechanical properties [J]. Materials Science and Engineering A, 2021, 826: 141985.
[24] ZHANG Luo, ZHU Hai-hong, LIU Jia-he, ZENG Xiao-yan. Track evolution and surface characteristics of selective laser melting Ti6Al4V [J]. Rapid Prototyping Journal, 2018, 24: 1554−1562.
[25] ABOULKHAIR N T, MASKERY I, TUCK C, ASHCROFT I, EVERITT N M. On the formation of AlSi10Mg single tracks and layers in selective laser melting: Microstructure and nano-mechanical properties [J]. Journal of Materials Processing Technology, 2016, 230: 88−98.
[26] FAN Zhi-qi, LU Ming-yuan, HUANG Han. Selective laser melting of alumina: A single track study [J]. Ceramics International, 2018, 44: 9484−9493.
[27] GUO Yue-ling, JIA Li-na, KONG Bin, WANG Na, ZHANG Hu. Single track and single layer formation in selective laser melting of niobium solid solution alloy [J]. Chinese Journal of Aeronautics, 2018, 31: 860−866.
[28] LIU Shuai, YANG Wen-sheng, SHI Xiao, LI Bin, DUAN Sheng-chao, GUO Han-jie, GUO Jing. Influence of laser process parameters on the densification, microstructure, and mechanical properties of a selective laser melted AZ61 magnesium alloy [J]. Journal of Alloys and Compounds, 2019, 808: 151160.
[29] GU D D, HAGEDORN Y C, MEINERS W, MENG G B, BATISTA R J S, WISSENBACH K, POPRAWE R. Densification behavior, microstructure evolution, and wear performance of selective laser melting processed commercially pure titanium [J]. Acta Materialia, 2012, 60: 3849−3860.
[30] SU Xu-bin, YANG Yong-qiang. Research on track overlapping during selective laser melting of powders [J]. Journal of Materials Processing Technology, 2012, 212: 2074−2079.
[31] MUGWAGWA L, YADROITSEV L I, MATOPE S. Effect of process parameters on residual stresses, distortions, and porosity in selective laser melting of maraging steel 300 [J]. Metals, 2019, 9: 1042.
[32] LESYK D A, MARTINEZ S, MORDYUK B N, DZHEMELINSKYI V V, LAMIKIZ A, PROKOPENKO G I. Post-processing of the Inconel 718 alloy parts fabricated by selective laser melting: Effects of mechanical surface treatments on surface topography, porosity, hardness and residual stress [J]. Surface and Coatings Technology, 2020, 381: 125136.
[33] ALI H, GHADBEIGI H, MUMTAZ K. Effect of scanning strategies on residual stress and mechanical properties of selective laser melted Ti6Al4V [J]. Materials Science and Engineering A, 2018, 712: 175−187.
[34] WEN P, JAUER L, VOSHAGE M, CHEN Y Z, POPRAWW R. SCHLEIFENBAUM J H. Densification behavior of pure Zn metal parts produced by selective laser melting for manufacturing biodegradable implants [J]. Journal of Materials Processing Technology, 2018, 258: 128−137.
[35] WEN Shi-feng, WANG Chong, ZHOU Yan, DUAN Long-chen, WEI Qing-song, YANG Shou-feng, SHI Yu-sheng. High-density tungsten fabricated by selective laser melting: Densification, microstructure, mechanical and thermal performance [J]. Optics and Laser Technology, 2019, 116: 128−138.

工艺参数对激光选区熔化成形纯镍表面质量及致密化行为的影响

岳天洋[1]，张 升[1,2]，王超越[3]，徐 伟[4]，徐一镝[1]，史玉升[5]，臧 勇[1,2]

1. 北京科技大学 机械工程学院，北京 100083；
2. 北京科技大学 顺德研究生院，佛山 528300；
3. 北京科技大学 材料科学与工程学院，北京 100083；
4. 北京科技大学 工程技术研究院，北京 100083；
5. 华中科技大学 材料科学与工程学院 材料成形与模具技术国家重点实验室，武汉 430074

摘 要：研究激光功率和扫描速度对激光选区熔化(SLM)成形纯镍的熔覆道特征、致密化行为和表面粗糙度的影响规律。结果表明，在一定范围内提升激光功率并降低扫描速度，可成形出连续、规则、光滑的熔覆道，这有助于抑制 SLM 成形过程中孔隙、球化等缺陷的形成。当扫描速度为 900 mm/s、激光功率为 255~275 W 时可获得最佳成形工艺窗口，此时，试样相对密度为 99.16%，抗拉强度为(360±2.747) MPa，上表面和侧表面的粗糙度分别为 (2.88 ±2.23) μm 和 (14.98 ±0.69) μm。

关键词：激光选区熔化；纯镍；熔覆道；致密化；表面粗糙度

(Edited by Bing YANG)